INSTITUTE OF PHYSICS PUBLISHING MEASUREMENT SCIENCE AND TECHNOLOGY
Meas. Sci. Technol. **15** (2004) 2333–2340 PII: S0957-0233(04)76170-6

Non-spherical seeding 3D positioning from CCD images using Lorenz–Mie theory

M Funes-Gallanzi[1], J A Guerrero[2], D Moreno[2], B Barrientos[2], F Mendoza Santoyo[2] and Guillermo García Torales[3]

[1] AVNTK SC, Guadalajara, Jalisco, Mexico
[2] Centro de Investigaciones en Optica AC, León, Guanajuato, Mexico
[3] CUCEI—Universidad de Guadalajara, Guadalajara, Jalisco, Mexico

E-mail: mfg@avntk.com

Received 8 February 2004, in final form 19 July 2004
Published 21 October 2004
Online at stacks.iop.org/MST/15/2333
doi:10.1088/0957-0233/15/11/020

Abstract
This paper describes the imaging of spherical and non-spherical particle diffraction patterns using plane-wave illumination. A discussion is presented on both the theoretical analysis of the diffraction pattern of the particle on its image plane using the Lorenz–Mie theory and its applicability to non-spherical particles. The images obtained for both spherical and non-spherical particles are quantitatively compared to calculated results, and implications for particle position estimation of non-spherical particles are discussed.

Keywords: diffraction pattern, non-spherical seeding, particle position estimation, PIV, velocimetry

(Some figures in this article are in colour only in the electronic version)

1. Introduction

Subsonic and transonic flows are of particular interest in the aerospace and power generation industries, which are constantly seeking improvements in efficiency, performance and reliability, while meeting increasingly tight regulations for engine noise and pollution parameters. In these types of flow, shock structures may be present and high-temperature gradients are common. A number of well-established non-intrusive optical diagnostic techniques for measuring such velocity fields require seed material to be entrained in the fluid to enable such measurements [1].

Various seeding materials are available for seeding purposes, the particular choice depending on the fluid properties and flow regime under study [2]. The techniques for dispersing and introducing the seed material into the flow are well known [3]. Seeding flows with particles to enable velocity measurements via laser Doppler anemometry/velocimetry or particle image velocimetry (PIV) techniques can be quite challenging, especially for the case of high-speed unsteady flows. Sharp velocity changes such as those found in shock structures put restrictions on the size and density of useful seeding material, making small seeding sizes a requirement in order to follow the flow accurately.

Polystyrene latex (PSL) spheres are a popular seeding material. They are easy to manufacture in large quantities to any size in the range of 0.3–10 μm [4]. PSL spheres are typically diluted to less than 1% in ethanol and introduced into the air flow upstream of the measurement station via an atomizer/spray nozzle. The ethanol quickly evaporates leaving the PSL spheres as a well-dispersed aerosol that then travels into the measurement region. A major drawback of PSL is its relatively low melting point of 100 °C, where it decrystallizes, maintaining its spherical shape if heavily cross-linked up to approximately 200 °C. At this higher temperature the material ceases to be spherical, becomes sticky and tends to agglomerate.

The challenges inherent in seeding flows are further compounded when high-temperature environments are encountered, where care must be taken to use refractory seed

material that will not degrade, melt or agglomerate. For high-temperature applications, a common seeding alternative is to generate a dry aerosol of metal oxide powder, which is then introduced into the facility upstream of the measurement region. Commercial grade alumina powder is often used in these cases. However, this material is not spherical.

Moreover, the study of two-phase flow composed of a liquid phase and a solid phase has many engineering applications, such as the transport of sediments in waterways, solid phase transport in tubing, fluidised beds, etc. This is an important application area for our research, where in general it requires 3D velocity field measurements, and where typically the solid phase is not made nor can be modelled by spherical seeding particles.

Recently, a new velocimetry method of 3D particle positioning from seeding particle images using generalized Lorenz–Mie theory has been reported [5–7]. This velocimetry method is applicable to the positioning of spherical seeding particles, illuminating the said seeding in backward or forward scattering mode. Another similar method is forward scattering particle image velocimetry [8].

It is well known that non-spherical particles exhibit a scattering field that is very close to that of the equivalent spherical particle on-axis, but differ significantly for larger angles [9]. Therefore, the question arises as to the applicability of using diffraction patterns for positioning non-spherical seeding, which would open the door to applying this method to high-temperature environments, sediment transport and complex two-phase flow problems, where non-spherical particles are often used. This matter is the overall subject of this work.

The case of spherical and non-spherical absorbing particles illuminated with monochromatic coherent light is considered. Two sets of image data were taken, one composed of spherical particle images ranging from -8.0 mm to $+8.0$ mm in 1.0 mm steps, while the other image data set was taken for identical conditions but for a non-spherical target seeding particle, whose average of the three main axes coincided with that of the spherical particle. The data obtained have been used to validate the applicability of a model originally produced for spherical particles to the scattering field of non-spherical particles.

2. Problem formulation

The authors decided to investigate the applicability of their 3D positioning method, which was originally produced to analyse spherical particles, to the case of non-spherical particles. In order to validate this approach, three steps were considered as fundamental in assessing the said method: possessing an accurate scattering theoretical model for spherical particles, a robust positioning algorithm capable of allocating accurate position estimates to arbitrarily positioned seeding particles and finally comparing the performance of the said algorithm using spherical seeding to its performance using non-spherical seeding.

The theory for a plane wave scattered by a spherical, isotropic, homogeneous, non-magnetic particle can be found in the literature [10, 11]. More advanced theoretical and experimental techniques may be used, but these depend on the solution to the general problem where the scattering centre is illuminated by an arbitrary laser beam, leading to generalized Lorenz–Mie Theory (GLMT) [12, 13]. Beginning with the classical treatment, the geometry for a simplified model was used. The experimental results using classical LMT treatment, however, proved insufficient to provide high accuracy 3D particle positioning and therefore the algorithm was extended to use a GLMT approach. This approach is thoroughly covered in a complementary article [6], where the full mathematical approach is described.

The experimental set-up and results compared to the calculations obtained from our GLMT code are fully described in [5]. For model verification purposes, a number of calculations were made, which were found to be in close agreement with other experimental/computational results. The method can also be used with images obtained from holographic PIV data or any method where particle images illuminated in a volume can be obtained, such as micro-fluids. However, in this case the illuminating wavefront is often spherical, a case also covered in a complementary article [14].

In the limit, since particles have to be small to follow high-speed flows accurately (conversely if large particles are used, the flow must be slow), and magnification must be low in order to accommodate adequate large investigation regions, seeding digital images are typically only a few pixels in diameter. When particles are illuminated in a volume, particle images are still small up to 25–30 pixels; for instance, when micron-sized particles used for high-speed flows are employed. To solve the problem by applying inverse-value techniques is theoretically possible, though there are stability issues, but it is very complex. A function-fitting approach comparing the radial intensity field of an experimental particle to a calculation is impractical. For instance, in order to obtain a 25-point vector of particle radial intensity, an image 50×50 pixels of the said particle needs to be recorded, that is to say a total of 2500 pixels. Therefore, an approach was used involving the generation of a calculated image and a direct comparison with an experimental image. In this way, if a 25×25 pixel image is generated, all 625 pixels will be used, thus allowing a higher accuracy at a lower magnification than otherwise available. The criterion employed for assessing the quality of the match between images was that of peak-signal-to-noise-ratio (PSNR) [15]. This is a very robust and sensitive measure of the difference between two images, given in dB. There are many versions of SNR ratios, but PSNR is very common in image processing, partly because it yields intuitively meaningful numbers.

The method initially used to make high-accuracy velocimetry measurements of three-dimensional space exploiting the scattered energy field and pattern-matching, employed a pre-processing step, estimation of the x and y particle position, the use of a neural net to estimate the z co-ordinate [8] and a non-linear optimization Nelder–Mead [16] position optimization subroutine using the first estimates previously derived for x, y and z. However, this approach proved unsuitable, as it only provided accuracy of the order of 200 μm at a magnification of $4\times$ and it was not robust enough to work in all conditions required. A recent refinement was the substitution of the neural net and Nelder–Mead modules for a single genetic algorithm module, whereupon accuracy

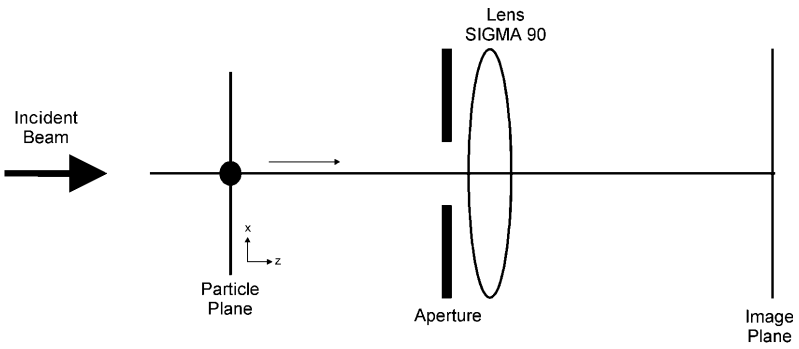

Figure 1. Forward scattering set-up for experimental image acquisition.

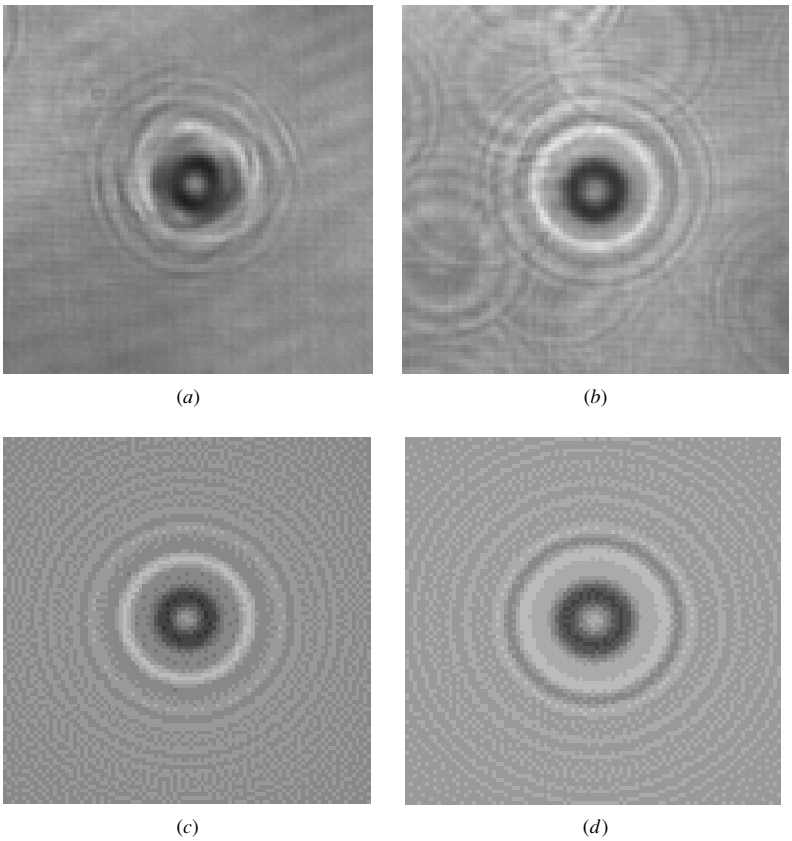

Figure 2. Images of silicate non-spherical (*a*) and glass spherical (*b*) particles at 2.5 mm after the focal plane, compared with their calculated estimates (*c*) and (*d*) respectively.

improved to around 100 μm immediately prior to the work being described in this paper. Genetic algorithms have been successfully used on otherwise intractable objective functions, such as those failing to satisfy continuity, differentiability, satisfaction of the Lipschitz condition, etc [17]. These algorithms maintain and manipulate a population of solutions and implement a 'survival of the fittest' strategy in their search for better solutions. This provides an implicit as well as an explicit parallelism that allows for the exploitation of several promising areas of the solution space simultaneously. The implicit parallelism is due to the schema theory developed by Holland [18], while the explicit parallelism arises from the manipulation of a population of possible solutions; the evaluation of the fitness of these solutions being easy to accomplish using parallel computing. Moreover, these algorithms can be hybridized with hill-climbing algorithms [19] to produce some of the fastest global optimization algorithms. The genetic algorithm used had the further advantage of not requiring the evaluation of all possible solution points. It merely used a random sampling as a starting population, and this was supplemented by increasingly fine detail in the regions that actually contained particles, each position being saved so it did not have to be recalculated. The details of this aspect of our research are reported elsewhere [21].

Finally, two image fields must be obtained and analysed using the same positioning algorithm. In this case, a silicate powder as normally employed for two-phase flow studies was used. This seeding typically contains particles that are highly non-spherical with an average of three principal axes. A

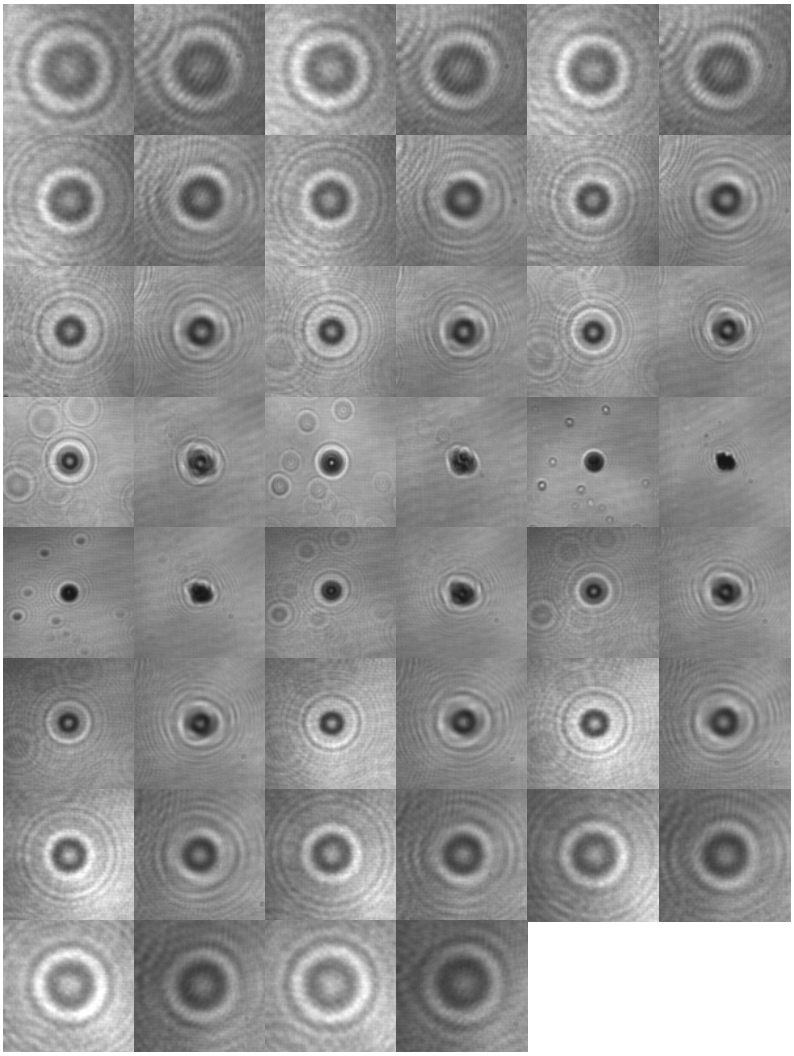

Figure 3. Spherical and non-spherical particle images for positions ranging from −8.0 mm to +8.0 mm about the focus plane (−8.0, −7.0, −6.0, −5.0, −4.0, −3.0,−2.5, −2.0, −1.5, −1.0, −0.5, focal plane, 0.5, 1.0, 1.5, 2.0, 2.5, 3.0, 4.0, 5.0, 6.0, 7.0, 8.0) to show similarities over the entire depth of field (the left image of each image pair is the spherical particle).

particle was selected for study, which had a mean diameter of 38 μm. This particle was moved using a linear displacement stage from −8.0 mm to +8.0 mm about the focal plane in steps of 1.0 mm. A second 38 μm diameter spherical particle made of glass was also moved through the same positions. The positioning algorithm was used on both data sets and the accuracy of the results was compared.

3. Experimental arrangement

The experimental set-up devised allows recording of forward scattering, as in [5]. Figure 1 shows the typical forward-scattering configuration. The slide used in the particle plane was antireflection coated to optimize the signal-to-noise ratio (SNR). A 10 mW He–Ne laser with a 4 mm beam diameter was used as the incident beam, the lens was the Cannon SIGMA 90, and the sensor was a 754 × 488 COHU CCD camera. Larger particle sizes were chosen for convenience of handling only, therefore, if the code could be validated for larger particles, it can also be applied to micrometre-sized particles, as are commonly employed in PIV.

4. Results and discussion

The first step in the research was to devise a method for working with small particles. The main problem to be solved is that of working with a single particle at a given time and at a fixed position in space, with a particle size measured with microscopic techniques.

Several methods for isolating a single particle were tried. A layer of monodisperse polystyrene spheres was deposited onto a slide, with a range of sizes from 3 to 13 μm tested. However, some problems were encountered because the solvent in which the polystyrene spheres were held evaporated, leaving cloudy contours on the slide surface. This noise precluded an accurate measurement of diffraction rings. Some were isolated and could be investigated but, when the defocus was increased, nearby particles caused problems. This approach was abandoned.

Glass particles not suspended in a solvent were used. These particles were deposited onto a slide and stuck to the glass surface by leaving some residual humidity on the slide. This arrangement worked well for large particle sizes. For

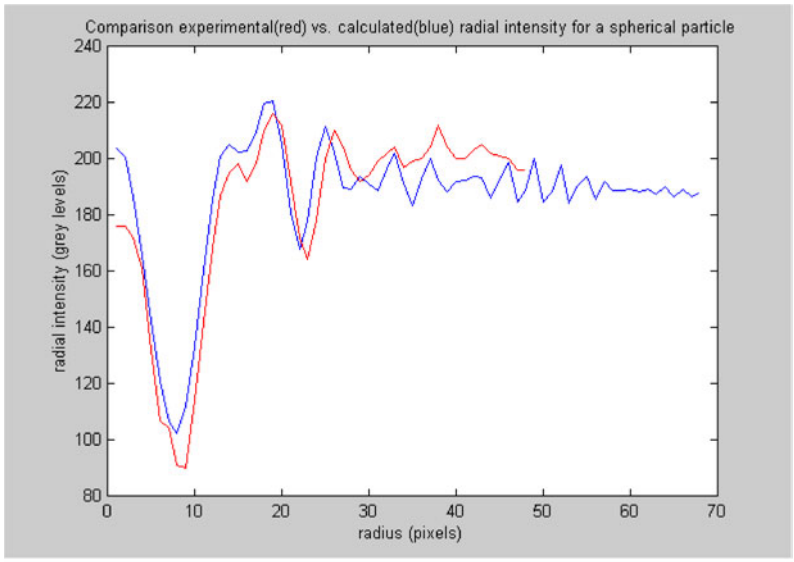

(*a*)

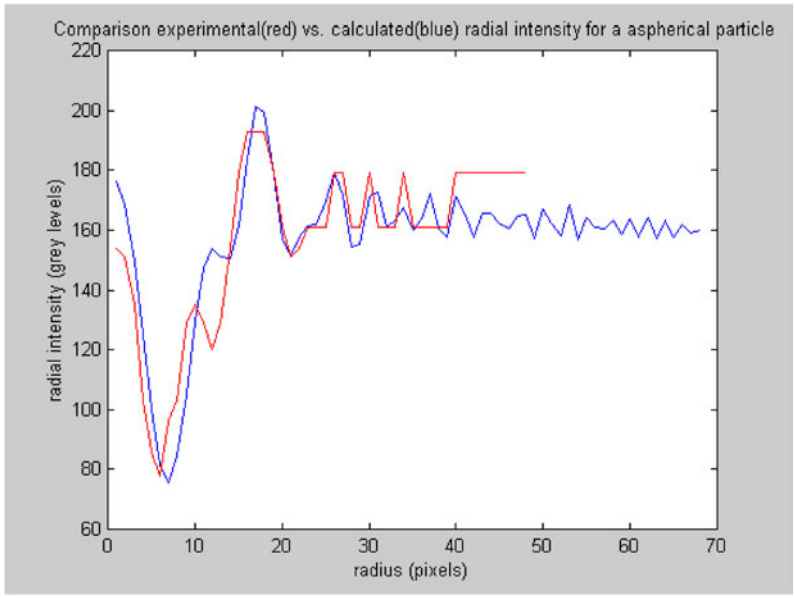

(*b*)

Figure 4. Radial intensity of spherical and non-spherical particles at 2.5 mm after the focal plane compared with calculated radial intensities.

smaller sizes, the system did not yield adequate ring definition due to noise. So, initially the larger 38 μm glass particles were selected. Then a non-spherical 38 μm mean diameter was selected from silica sand particles. To get the 38 μm for non-spherical particles, an average diameter measurement along the particle's main axes was calculated. The aspect ratio of the aspherical particles was of the order of 1:1.5, which is a moderate degree of asymmetry. The technique would therefore be suitable for seeding made up of asymmetry of this order of magnitude, but would not be viable in cases of extreme asymmetry of the order of 1:3 or more, as can be found, for instance, in aluminium silicate.

The set-up consisted of an arrangement with the particle set at an object distance of 468.33 mm, an image distance of 111.4 mm yielding a magnification of $1/4.2$, $f/\#2.8$, laser frequency of 632.8 nm with a power level of 10 mW and a beam diameter of 4 mm, a 90 mm SIGMA lens, where the glass and silica sand particles were considered to have a complex refractive index of $1.46+i3.0 \times 10^{-7}$ and $1.57+i1.0 \times 10^{-4}$, respectively.

In comparing the results of the calculated focus position and that experimentally measured, an offset of 1.75 mm was found, which was adjusted throughout these calculations.

Figure 2 shows the comparison of non-spherical (*a*) and spherical (*b*) particles at a magnification of $4 \times$ and -2.5 mm focal distance and physical parameters as stated above, with their calculated representations (*c*) and (*d*) respectively. The apparent difference between the two calculated images is due to the offset and to the differing complex index of refraction employed to represent both materials.

Tests were carried out for different defocus positions and figure 3 shows pair comparisons between spherical and

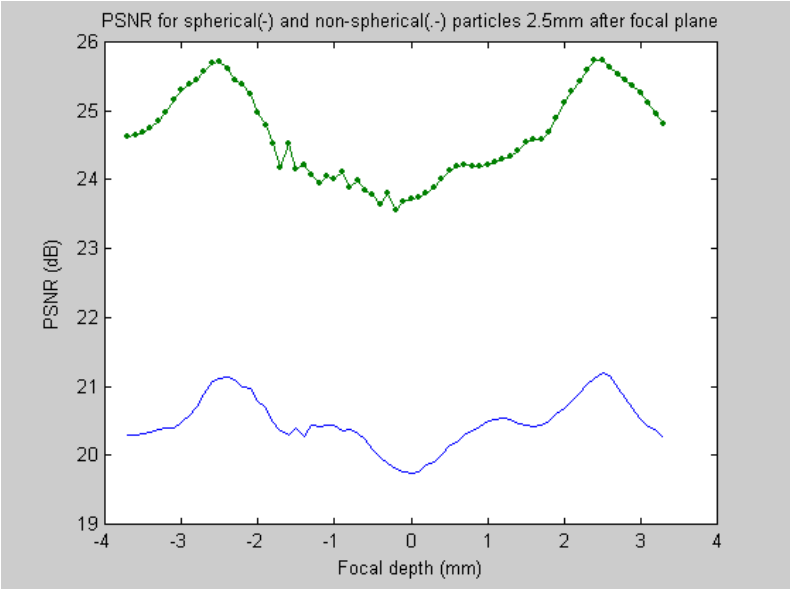

Figure 5. PSNR as a function of depth for spherical and non-spherical particles 2.5 mm after the focal plane.

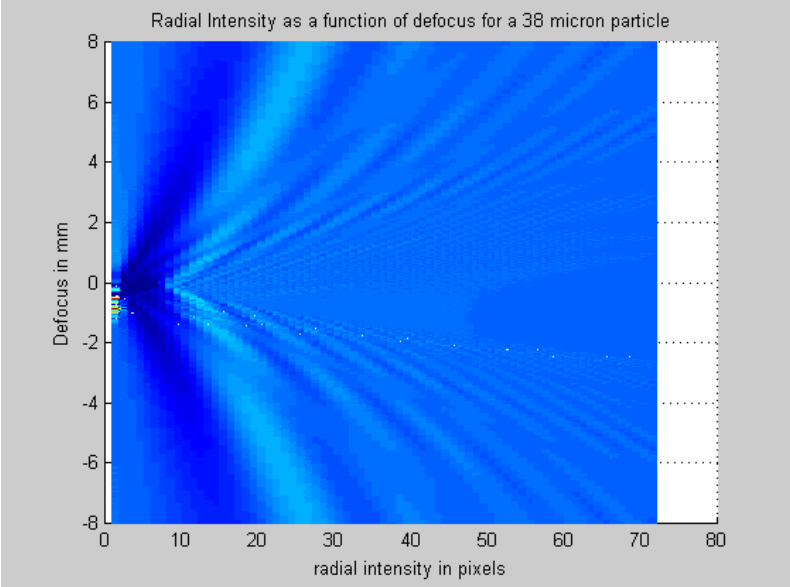

Figure 6. Radial intensity of a spherical glass particle over the working depth −8 to +8 mm.

non-spherical pattern diffraction. The defocus position ranged from −8.0 mm to +8 mm. Some images are brighter than others due to a little misalignment of the system, the only difference is a constant illumination factor between pairs.

A radial intensity comparison for a spherical and non-spherical particle at 2.5 mm after the focal plane with its calculated representation is shown in figures 4(*a*) and (*b*), these being radial plots of the images shown in figure 2. The difference in the calculated profiles is due to the differing indices of refraction. Nevertheless, they can be seen to be good approximations to the experimental data, though only one of the experimental radial directions is shown for clarity in each case.

Figure 5 shows a plot of the peak-signal-to-noise ratio as spherical and non-spherical particle images at 2.5 mm were compared to those in the range from −3.5 to +3.5 mm. As expected, only two peaks exist at −2.5 and +2.5 mm, with that at +2.5 mm being the overall maximum because although equidistant images from the focal plane have very similar images, they do differ enough for the software to differentiate them. It ought to be pointed out that the absolute PSNR over the range of interest is higher in the case of the non-spherical particle than in the spherical case. This was due to an uneven illumination of the spherical particle and the presence of some small particles, the combination of which lowers the image quality of the spherical particle. On the other hand, the non-spherical particle benefits from a more even illumination and no other sources of noise and therefore records a higher PSNR when compared to the calculated image.

Figure 6 shows the calculated radial intensity of the spherical particles in the range from −8 to +8 mm. The calibration procedure proved to be crucial to an accurate

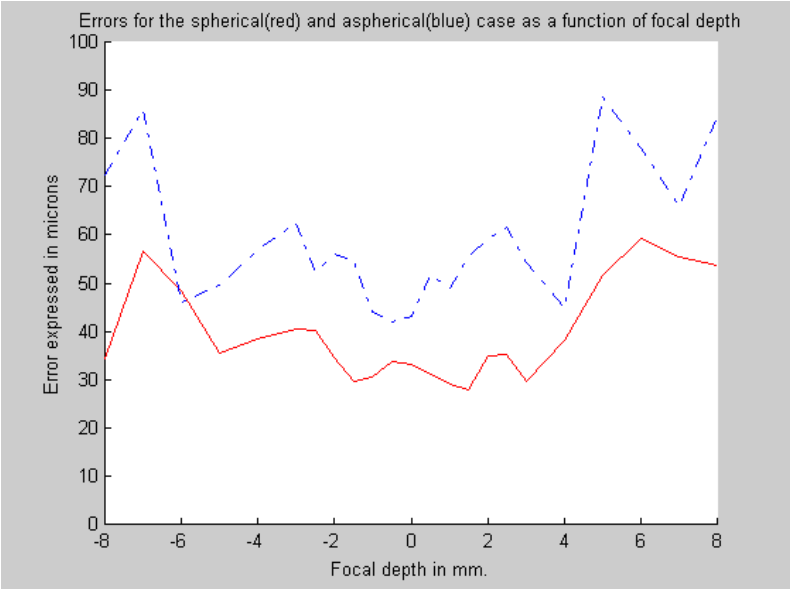

Figure 7. Sample run positional errors expressed in microns for particles shown in figure 3 using the algorithm described in this paper.

working of this algorithm. As can be seen from figure 6, particles have over some ranges basically the same profile which only changes in scale as the particle is moved along the z direction. Therefore, accurate scaling in terms of pixel size, magnification, etc directly impacts the accuracy of the method. In this configuration, i.e. forward scattering, it was relatively easy to calibrate the energy falling on the CCD. However, in side or back scattering this calibration step would be more challenging.

For the non-spherical case, it is interesting to note that although the image quality is severely degraded by non-sphericity, the symmetry position is not substantially altered, which results in a mean positioning accuracy of 60 μm for non-spherical particles compared to 40 μm (i.e., approximately one particle diameter) for the spherical case.

Figure 7 shows these results in somewhat more detail. A sample run result is shown therein where positional errors are expressed in microns for particles shown in figure 3 using the algorithm described in this paper. Clearly, there is a wide variation from particle to particle, which is due we believe to the genetic algorithm not having been optimized yet. This is part of the work currently in progress.

5. Conclusions

The importance of considering the applicability of algorithms developed for spherical particles to the case of non-spherical seeding particles has been illustrated.

Much work remains in refining code, improving the particle image digital representation, obtaining accurate complex indices of refraction for the seeding used, speeding it up and extending it; so all forms of aberrations may be considered. However, having a quantitatively accurate particle image positioning algorithm even for non-spherical particles is a significant step in velocimetry applications. A further area of research currently under way is the simultaneous positioning and particle sizing, as often tracer particle size also needs to be established. This step opens the way for routine accurate 3D velocity estimation, by 3D particle positioning from 2D camera images, even when doing high-temperature velocimetry work using non-spherical particles.

The image data sets of both spherical and non-spherical seeding particles were analysed using a GLMT code, yielding an error of 40 μm for the spherical seeding, and an error of 60 μm for the non-spherical seeding particles, in a working depth of 16 mm. Therefore, we can conclude that code developed for positioning spherical seeding particles can also be used for non-spherical seeding particles in cases where non-spherical seeding needs to be visualized, such as high-temperature PIV where non-spherical seeding is used, sediment transport and combustion studies, albeit at the cost of a drop in positioning accuracy.

Acknowledgment

Dr Marcelo Funes-Gallanzi wishes to acknowledge support for this research by CONACyT-Mexico under contract 35062-E.

References

[1] Adrian R J and Yao C S 1985 Pulsed laser technique application to liquid and gaseous flows and the scattering power of seed materials *Appl. Opt.* **24** 44–52

[2] Meyers J F 1991 *Generation of Particles and Seeding (Von Karman Institute Lecture Series 1991-08)*

[3] Melling A 1997 Tracer particles and seeding for particle image velocimetry *Meas. Sci. Technol.* **8** 1406–16

[4] Nichols C E 1987 *Preparation of Polystyrene Microspheres for Laser Velocimetry in Wind Tunnels* NASA TM-89163

[5] Guerrero A, Mendoza Santoyo F, Moreno D, Funes-Gallanzi M and Fernandez S 2000 Particle positioning from CCD images: experiments and comparison to the generalized Lorenz–Mie theory *Meas. Sci. Technol.* **11** 568–75

[6] Moreno D, Mendoza Santoyo F, Funes-Gallanzi M and Guerrero J A 2000 Particle positioning from a single CCD image for application to velocimetry: theory and comparison to experiment *Appl. Opt.* **39** 5117–24

[7] Funes-Gallanzi M 2000 Tunnelling velocimetry: consilience comes to the study of fluid dynamics *10th Int. Symp. on Applications of Laser Techniques to Fluid Mechanics (Instituto Superior Tecnico, Ladoan, 10–13 July 2000)*

[8] Ovryn B, Wright T and Khaydarov D 1995 Measurement of three-dimensional profiles using forward scattering particle image velocimetry and neural net pattern recognition *SPIE* **2546** 112–23

[9] Bohren C F and Huffman D R 1983 *Absorption and Scattering of Light by Small Particles* (New York: Wiley)

[10] Debye P 1909 Der Lichtdruck auf Kugeln von beliebigem Material *Ann. Phys., Lpz.* **30** 57–136

[11] Mie G 1908 Beiträge zur Optik trüber Medien, speziell kolloidaler Metallösungen *Ann. Phys., Lpz.* **25** 77–445

[12] Gouesbet G and Gréhan G 1982 Sur la généralisation de la théorie de Lorenz–Mie *J. Opt. (Paris)* **13** 97–103

[13] Gouesbet G, Maheu B and Gréhan G 1988 Light scattering from a sphere arbitrarily located in a Gaussian beam, using a Bromwich formulation *J. Opt. Soc. Am.* A **5** 1427–43

[14] Guerrero J A, Mendoza Santoyo F, Moreno D and Funes-Gallanzi M 2002 The case of a spherical wavefront for the generalized Lorenz–Mie theory including a comparison to experimental data *Opt. Commun.* **203** 175–82

[15] Yuval Fisher *et al* 1995 *Fractal Image Compression* (Berlin: Springer) section 2.4, Pixelized data

[16] Wright M H The Nelder–Mead method: numerical experimentation and algorithmic improvements *AT&T Bell Laboratories Technical Report,* Murray Hill, NJ

[17] Davis L 1991 *Handbook of Genetic Algorithms* (New York: Van Nostrand Reinhold)

[18] Holland J 1975 *Adaptation in Natural and Artificial Systems* (Ann Arbor, MI: The University of Michigan Press)

[19] Bersini H and Renders B 1994 Hybridising genetic algorithms with hill-climbing methods for global optimizations: two possible ways *IEEE Int. Symp. on Evolutionary Computation (Orlando, FL)* pp 312–7

[20] Padilla Sosa P, Valdez J E, Berriel L R, Sahagún Ortiz L R and Funes-Gallanzi M 2003 Robust genetic algorithm for high-accuracy particle position in three-dimensional particle image velocimetry applications *Opt. Eng.* **42** 459–66